

# Life and death of a fakir droplet: Impalement transitions on superhydrophobic surfaces

S. Moulinet<sup>1,a</sup> and D. Bartolo<sup>2,b</sup>

<sup>1</sup> Université Paris 6, Laboratoire de Physique Statistique de l'Ecole Normale Supérieure, UMR 8550 (CNRS, ENS, P6, P7), 24 rue Lhomond, 75231 Paris cedex 05, France

<sup>2</sup> Laboratoire de Physique et de Mécanique des Milieux Hétérogènes, PMMH, ESPCI, Paris 6, Paris 7, UMR CNRS 7636, 10 rue Vauquelin 75231 Paris cedex 05, France

Received 19 June 2007 and Received in final form 3 October 2007

Published online: 5 December 2007 – © EDP Sciences / Società Italiana di Fisica / Springer-Verlag 2007

**Abstract.** We show that the equilibrium state of a water drop deposited on a superhydrophobic surface cannot be solely determined by its macroscopic contact angle but also depends on the drop size. Following the evolution of the interface of evaporating droplets, we demonstrate that the liquid can explore a succession of equilibrium conformations which are neither of the usual fakir nor Wenzel types. A comprehensive description of the transition between these wetting states is provided. To do so, we have taken advantage of microfabrication techniques and interference microscopy which allows for the “3D” imaging of the liquid interface. In addition, we propose a simple theoretical description of the interface geometry which goes beyond the standard two-state picture for superhydrophobicity. This model accounts correctly for all our experimental observations. Finally, guided by potential microfluidic applications we propose an efficient design strategy to build robust liquid repellent surfaces.

**PACS.** 47.55.dr Drops and bubbles: Interactions with surfaces – 68.08.Bc Wetting

## 1 Introduction

During the last decade, much effort has been devoted to mimic the extreme hydrophobic properties of various bio-surfaces such as plant leaves or insects wings and legs [1–3]. These so-called superhydrophobic surfaces share two common features: they are made of (or covered by) hydrophobic materials, and are textured at the micron and, or, sub-micron scales. Water drops either bounce or roll off these water-repellant surfaces, making liquid deposition almost impossible. From a practical point of view, potential applications of artificial superhydrophobic surfaces include self-cleaning coating for clothes or glass, antibiofouling paintings, drop transport on lab on a chip devices and turbulent drag reduction [4,5]. However only few commercial superhydrophobic products are available due to the difficulty to design robust superhydrophobic coatings though hundreds of processes have been proposed to build microscopically rough surfaces out of hydrophobic materials [5–7]. From a fundamental point of view significant efforts have been made to study the dynamics of fluids flows in the vicinity of hydrophobic rough surfaces. But, suprisingly, the current understanding of the static

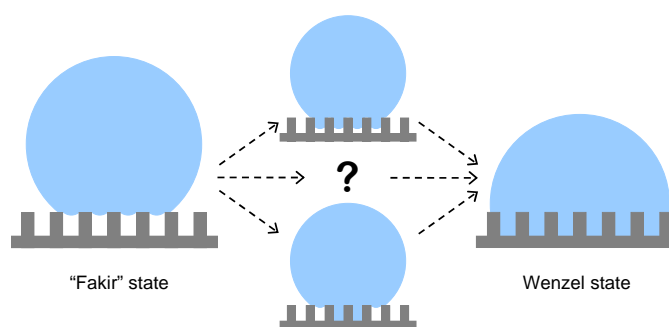


**Fig. 1.** Schematic representation of the two well-known wetting states of a drop on a hydrophobic structured surface. We call the transition from the fakir to the Wenzel state “impalement transition”. The aim of this present work is to reveal the existence of other stable conformations prior to impalement.

wetting properties of superhydrophobic surfaces remains quite superficial.

We first recall briefly the standard paradigm to account for superhydrophobicity (see [7] for a recent review). The two different wetting states that can be observed on microstructured hydrophobic surfaces are sketched in Figure 1. i) Wenzel state: the liquid follows the topography of

<sup>a</sup> e-mail: [sebastien.moulinet@lps.ens.fr](mailto:sebastien.moulinet@lps.ens.fr)

<sup>b</sup> e-mail: [denis.bartolo@espci.fr](mailto:denis.bartolo@espci.fr)

the solid. Defining the surface roughness  $\zeta$  as the ratio between the area of the areal surface over the apparent surface area, the equilibrium contact angle of a liquid drop is given by  $\cos(\theta) = \zeta \cos(\theta_{\text{flat}})$ , where  $\theta_{\text{flat}}$  is the Young contact angle on a flat surface. ii) Fakir state: The liquid rests on the top of the surface asperities, air pockets remain trapped between the solid and the liquid surface. Only a fraction  $\phi$  of the solid surface is in contact with the liquid. Fakir drops adopt a contact angle given by the weighted sum  $\cos \theta_{\text{fakir}} = \phi \cos \theta_{\text{flat}} - (1 - \phi)$ , (Cassie-Baxter average). It can be easily shown that the drop minimizes its surface energy in the fakir (respectively Wenzel) regime if  $\zeta$  is larger (respectively smaller) than  $\cos \theta_{\text{fakir}} / \cos \theta_{\text{flat}}$ . Consequently, fakir droplets should be observed only on ultra rough substrates. This standard approach based on energy minimization cannot describe the potential metastability of fakir or Wenzel states. Several studies have recently shown that both the measured average contact angle and the contact angle hysteresis on superhydrophobic surfaces strongly depends on the way the liquid has been deposited [8–12]. This demonstrate the existence of metastable wetting states. Precisely, it has been reported in [9, 13, 12] that an increase of the pressure in the drop can trigger an irreversible impalement transition to the Wenzel state. Except for the simplified case of the 1D surface geometry [14, 15], all the models proposed to account for this transition require the *a priori* knowledge of the deformation pathway followed by the liquid interface during the impalement process, see Figure 1 [12, 16–18].

In this paper, we focus on pressure-driven transitions of slowly evaporating droplets. We combine two optical techniques to observe the full 3D shape of a drop deposited on a model superhydrophobic surface and provide a quantitative description of the impalement scenario of fakir droplets. Thanks to this technique we relate the deformation of the water interface to the internal Laplace pressure. The drop can follow two successive deformations sequences prior to impalement. First, the fakir drop remains on top of the asperities of the rough surface and increases its curvature as the drop evaporates. Then, impalement is locally nucleated by a defect and lead to the growth of a partly impaled region below the drop where the liquid wets the sides of substrate's asperities. The drop thus adopts a succession of new equilibrium conformations that do not correspond to the standard fakir and Wenzel cases. Eventually, when the liquid touches the basal surface of the substrate, the drop fully wets the solid and reach the Wenzel state. We present a simplified model that accounts for the observed heterogeneous impalement scenarios. Finally, on the basis of this model, we propose an efficient design strategy for ultra robust superhydrophobic surfaces on which arbitrarily small fakir droplets can be deposited and transported.

## 2 Real-time imaging of drop impalement

The experiment consists in gently depositing a millimetric water droplet in the fakir state on a superhydrophobic

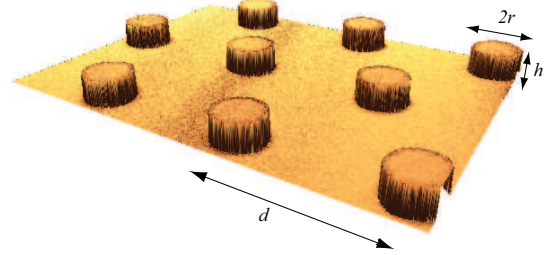


**Fig. 2.** Micropatterned PDMS surface. Image obtained with an optical profilometer (FOGALE nanotech). The pitch of the triangular lattice is  $d = 50 \mu\text{m}$ .

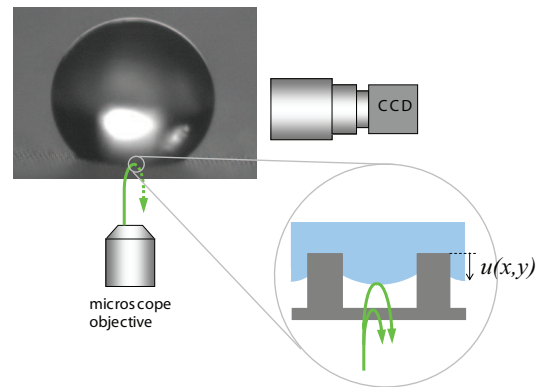


**Fig. 3.** Schematic representation of the experimental setup. An evaporating drop is simultaneously observed with: i) a standard CCD camera equipped with a macro objective and ii) with an inverted microscope. Closeup: gray on-line: solid surface, blue on-line: liquid.  $u(x, y)$  is the liquid-air interface profile. The arrows sketch the two optical paths that interfere to form the RICM patterns.

substrate and simply let it evaporate at room temperature. The typical evaporation time is  $\sim 90$  min. All the experiments have been performed on thin PDMS (Poly-Dimethyl Siloxane) hydrophobic surfaces microstructured using replica molding techniques [19]. The primary molds are made by UV lithography of SU8 photoresist resin (Microchem Corp.). The patterns are triangular arrays of cylindrical pillars with a pitch  $d = 50 \mu\text{m}$  (see Fig. 2). We have used several surfaces with pillars of radius  $r = 10 \pm 2 \mu\text{m}$ . Two different pillars' height have been used:  $h = 13$  and  $h = 9.5 \mu\text{m}$ . We have also taken advantage of UV lithography to build defective arrays including isolated missing pillars.

### 2.1 Macroscopic observation: fakir to Wenzel transition

We combine two optical techniques to observe the full 3D shape of a drop, see Figure 3. The PDMS substrate supporting the fakir drop is positioned on an inverted microscope. The sample is lighted through the objective with a monochromatic light using a halogen light bulb and a narrow interferometric filter (wave length:  $\lambda = 520$  nm,

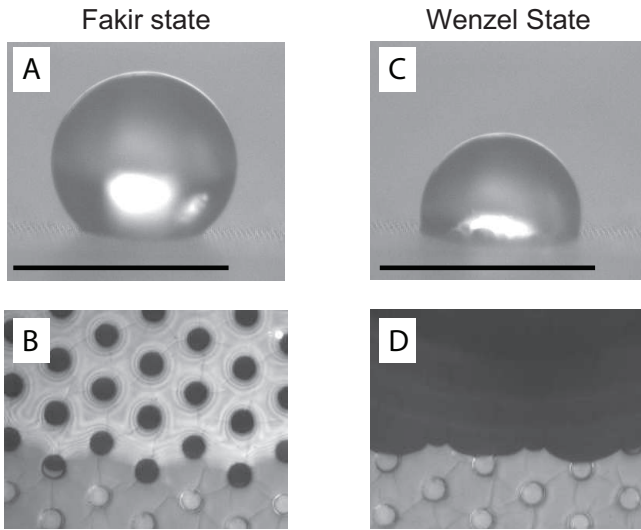


**Fig. 4.** A) Fakir water drop on a textured PDMS surface, side view. Scale bar 1 mm. B) Fakir water drop, RICM picture taken at the macroscopic contact line. The black regions correspond to water-PDMS interfaces, lighter regions to air-water interfaces. The fringes below the drop indicate that the drop is only in contact with the top of the PDMS pillars. C) Same drop as in A, picture taken 1 min later. The drop is now in the Wenzel state. Note the reduction of the contact angle and the advancing of the contact line. Scale bar 1 mm. D) RICM picture of a Wenzel drop. The liquid fully covers the patterned surface.

band width:  $\Delta\lambda = 6$  nm). The air-water interface below the drop is observed by reflection interference contrast microscopy (RICM) through the transparent PDMS surface. A change of the interference pattern intensity from a maximum to a minimum, corresponds to a variation of  $\lambda/4 = 130$  nm of the distance  $u$  between the drop surface and the top of the pillars. This simple rule leads to a straightforward reconstruction of the three-dimensional shape of the interface. Simultaneously, the temporal evolution of the drop radius,  $R_d$  is directly monitored with a CCD camera.

When a water drop is gently deposited on the PDMS superhydrophobic surface, the macroscopic contact angle exceeds  $140^\circ$ . Note that this value is much higher than the advancing contact angle measured on a flat PDMS substrate ( $\sim 110^\circ$ ). The RICM pictures show that the liquid is supported by the top of pillars, Figure 4B. The drop is in the fakir state. As the drops evaporates, its radius decreases. After a few minutes, the drops adopts its receding contact angle ( $\sim 140^\circ$ ), Figure 4A, and the contact line of the fakir drop starts retracting. A sharp transition is observed when the drop radius reaches a critical value which depends on the pattern geometry. The contact line suddenly jumps forward, the contact angle drops down to a smaller value, Figure 4C, and the RICM interference pattern becomes uniformly dark, Figure 4D. These three observations illustrate the transition to the Wenzel state. This transition occurs in less than 20 milliseconds. Once the drop is impaled on the PDMS pillars, the contact line remains pinned until evaporation is completed.

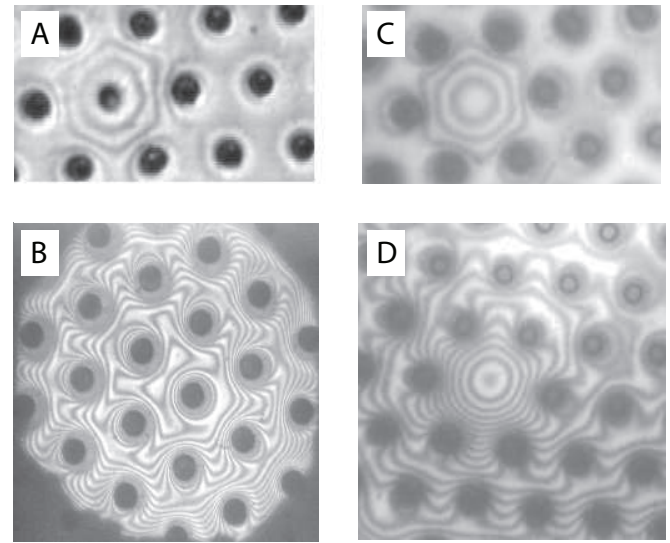


**Fig. 5.** RICM picture of a drop deposited on perfect arrays (A and B) and on arrays with isolated missing pillars (C and D). A) Localized defect. The interface is penetrated by a single pillar. Image taken just after the drop deposition  $P_L \sim 140$  Pa. B) Partly impaled droplet taken few minutes prior to the Wenzel transition,  $P_L = 280$  Pa. C) Isolated missing pillar. Image taken just after the drop deposition, the drop is in a fakir state. D) Partly impaled droplet. The pillars around the localized defects have penetrated the interface,  $P_L = 260$  Pa. On the four pictures the pitch of the lattice is  $d = 50 \mu\text{m}$ .

## 2.2 RICM imaging: Partial impalement of fakir droplets and nucleation scenario

We now describe in detail the impalement scenario uncovered by the RICM pictures, see, *e.g.*, Figure 5. We have reconstructed the profiles of the free surface,  $u(x, y)$ , along a principal direction of the triangular lattice. In Figure 6 we show, for two different experiments, the deformations of the interface when the liquid evaporates. Just after drop deposition, the liquid interface adopts the shape of a tent roof supported by all the pillars, Figure 6. As the drop evaporates the liquid penetration increases since the curvature increases. However the penetration remains identical in each cell of the triangular lattice. Below a critical radius that may vary from one experiment to the other, one pillar suddenly pierces the interface. The drop is no longer in the fakir state. The RICM pattern associated with a localized impalement event is shown in Figure 5A. However, the location of this pillar cannot be *a priori* predicted. To circumvent this experimental difficulty, we have used surfaces patterned with arrays containing imperfections such as isolated missing pillars, Figure 5C and D. This allows to enforce the location of the nucleation point from which the partly impaled region grows. We can infer from the RICM pictures, Figure 5B and D, and from the interface profiles, Figure 6A, that as the drop curvature increases the pillars surrounding the defect start being wetted. This partly impaled region grows and can even reach the edge of the drop as illustrated by the profiles plotted in Figure 6B. Though all the pillars

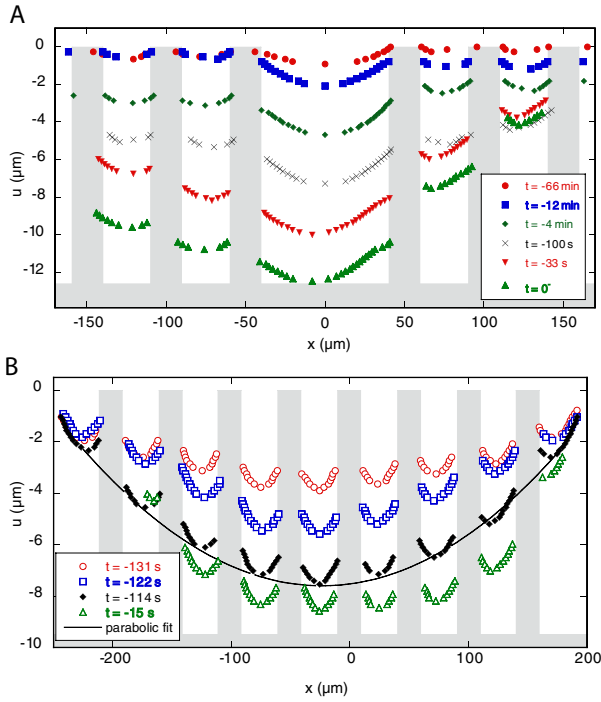


**Fig. 6.** Profiles of the water interface ( $t = 0$  corresponds to the impalement transition to the Wenzel state). The gray patterns sketches the solid substrate. A) Patterned surface with one missing pillar. B) Array without defects. The solid line is a parabolic fit of the envelop of the profile 114s prior to the Wenzel transition.

supporting the liquid are partly wetted, the drop has not yet reached the Wenzel state. As soon as the maximal penetration  $p(t) \equiv \max_{x,y} |u(x, y; t)|$  becomes equal to the pillars height,  $h$ , the liquid-air interface contacts the basal surface of the solid. This event triggers a sharp transition to the Wenzel state.

Given the above description, the maximal penetration  $p$  of the liquid interface appears to be a natural control parameter to describe the impalement transition. In all that follows we will use the Laplace pressure  $P_L \equiv 2\gamma/R_d$  instead of the drop radius to describe the equilibrium wetting state of the liquid. We have demonstrated in a previous study that impalement is generically induced by an increase of pressure in the drop [12]. In Figure 7 we plot the evolution of  $p$  with  $P_L$ . At low  $P_L$ , the drop is in the fakir state and  $p$  increases linearly with the pressure. As the pillars start penetrating the liquid the slope of the  $(P_L, p)$  curves sharply increases. For the profiles plotted in Figure 7A, this second regime ends at high pressure when  $p = h$  this, again, corresponds to the Wenzel transition. More surprisingly a third regime is observed on Figure 7B which corresponds to experiments done on a defect-free surface. In this case, at high Laplace pressure, the variations of the penetration with the Laplace pressure are strongly slowed down prior to the Wenzel transition. The analysis of a single interface profile cannot tell whether the drop is in the second or the third regime uncovered by the penetration plot, the drop remain partly impaled on the pillars.

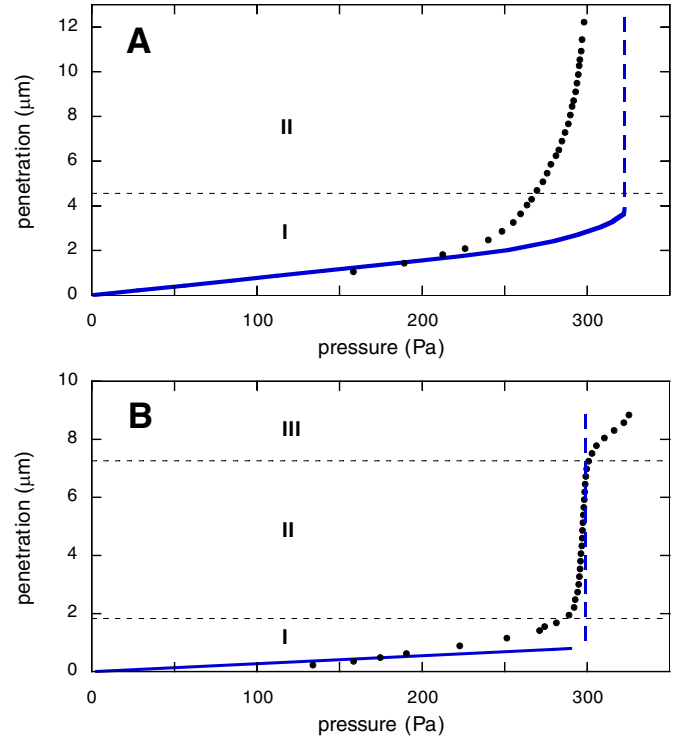


**Fig. 7.** Penetration *versus* Laplace pressure, experimental (circles) and numerical data (full lines). The vertical dashed lines correspond to the sliding pressure defined in equation (3) with  $\theta_a = 98^\circ$ . This value corresponds to the contact angle on the side of the pillars measured on Figure. 6. The last experimental point corresponds to the image taken just before to the transition to the Wenzel state. A) substrate with a missing pillar. B) substrate without defect.

Before closing this section, we add two comments:

- We have carefully checked that the radius of curvature of the interface measured in Figure 6 at the maximal penetration is equal to the measured macroscopic drop radius  $R_d$ . This demonstrates that the free surface adopts a constant curvature equilibrium shape. To further check this important point we have plotted the evolution of the radius  $R_d(t)$  and the maximal penetration,  $p(t)$ , Figure 8. At the beginning of the experiment the penetration of the liquid increases slowly. Then the velocity of the penetration increases quite sharply  $\approx -10$  min prior to impalement. For the experiment corresponding to Figure 8 the maximal penetration velocity is  $\sim 0.7 \mu\text{m/s}$ . We conclude unambiguously from this small value that the dynamic of the interface is quasi-static. As a matter of fact, the deformation of the interface propagates at a much higher velocity, typically of order  $\sqrt{\gamma/\rho\delta} \sim 2 \text{ m/s}$  (respectively  $\gamma/\eta \sim 70 \text{ m/s}$ ) in the inertial (respectively viscous) limit where  $\gamma$  is the surface tension,  $\rho$  the liquid density,  $\eta$  the viscosity and  $\delta$  a typical length scale set by the lattice spacing; here  $\gamma = 70 \text{ mN/m}$ ,  $\rho = 10^3 \text{ kg/m}^3$ ,  $\eta = 10^{-3} \text{ Pa} \cdot \text{s}$  and  $\delta$  has been taken equal to 10 microns.

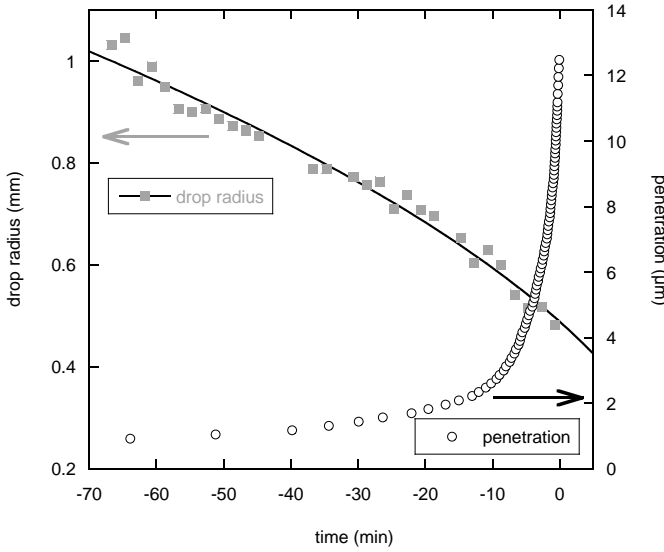


**Fig. 8.** Drop radius and maximal penetration *versus* time for an experiment on a surface containing missing pillars. The kinetic of the drop evaporation is consistent with the well-known  $R_d \sim |t - t_0|^{1/2}$  scaling law (solid line) for aerosols and drops lying on flat non-wetting surfaces [20].

- When the interface is pushed downward, the liquid slides along the pillars. This is consistent with the evolution of the contact angle along the side walls of the pillars. On Figure 6 we can notice that the local contact angle increases as  $R_d$  decreases until the top of a pillar penetrates the water. Thereafter the local angle then remains constant and equal to  $100 \pm 3^\circ$ , a value close to  $\theta_a$ .

In summary of our main experimental results: when a fakir drop evaporates, the decrease of its radius induces a transition to a Wenzel state. Beyond this simple macroscopic observation, RICM has brought an important new insight to the impalement transition: the drop explores a succession of equilibrium shapes that belong neither of the fakir nor of the Wenzel class. These new wetting conformations cannot be uncovered solely by the standard macroscopic contact angle measurement. For all the partly impaled states, the drop makes a contact angle very close to  $\theta_{\text{fakir}}$ . Finally, plotting the penetration curves (penetration *versus* Laplace pressure) we have identified three main different impalement regimes which we study in details below.

### 3 Pressure-induced impalement: theoretical description

In this section we construct a simple model to describe the outcome of a fakir droplet evaporating on model superhydrophobic surface. We especially focus on the evolution of the maximal penetration  $p$  with the inner Laplace pressure (or equivalently with the evaporating drop radius), Figure 7. We first recall and complete the simple mean-field approach presented in [12]. For the sake of clarity,

this model is detailed only for the surface pattern corresponding to our experiments.

We assume that the penetration field has the same symmetries as the pillars lattice. The free surface enclosed by all the elementary cells experiences a force  $P_L[A(1 - \phi)]$ , where  $A$  is the projected area of one cell and  $\phi = (2\pi/\sqrt{3})(r/d)^2$  is the pillar density for a triangular lattice. At mechanical equilibrium, this force is balanced by the capillary force  $N_p f$  applied at the top of  $N_p = \phi A/\pi r^2$  pillars in the cell. The elementary force  $f$  is given by  $f \equiv [2\pi\gamma r \cos(\theta)]$  where  $\theta$  is the “average” contact angle defined on the pillars sides. At equilibrium the force balance equation is

$$P_L = \frac{2\phi}{1 - \phi} |\cos(\theta)| \frac{\gamma}{r}. \quad (1)$$

Note that all the information on the shape of the interface is encoded in the  $\cos(\theta)$  prefactor. In the low- $\phi$  limit, and for small surface deformations (*i.e.* at low  $P_L$ ),  $\cos[\theta(p)] \sim p/r$  (omitting logarithmic corrections), which is a well-known result in the context of thin fibers wetting [21]. It then follows from equation (1) that the penetration scales linearly with the pressure applied of the interface:

$$p \sim d \frac{P_L}{(\gamma/d)}. \quad (2)$$

This simple model also predicts the existence of a critical pressure above which fakir drops cannot be observed. The contact angle  $\theta(p)$  is indeed bounded by the local advancing contact angle  $\theta_a$ . Hence, if  $\theta(p) > \theta_a$ , the above force balance equation has no solution and the contact line will spontaneously slide along the pillars down to the basal surface. This would induce the Wenzel transition. This sliding scenario should occur at the critical pressure:

$$P_{\text{sliding}} = \frac{2\phi}{1 - \phi} |\cos(\theta_a)| \frac{\gamma}{r}. \quad (3)$$

The global trends of the experimental penetration curve are correctly predicted by this scaling model, see Figure 7A: at low pressure the penetration of the fakir drop increases linearly with  $P_L$  and abruptly increases as the pillars penetrate the interface.

To go beyond scaling arguments, we have solved numerically the Laplace equation for the penetration field,  $u(x, y)$  on an elementary rectangular cell including two perfect pillars with periodic boundary conditions. The details of the numerical method are provided in appendix. The computed penetration is plotted *versus* pressure for different advancing contact angles in Figure 9. These plots indicate that the linear approximation at low pressure is excellent. The penetration curves are indeed very well described by straight lines with slopes independent of the advancing contact angle. In addition, above a critical pressure, the contact lines along the pillars moves toward the bottom of the calculation box after each intermediary steps of the numerical resolution. The divergence of the calculation indicates that no equilibrium solution exists

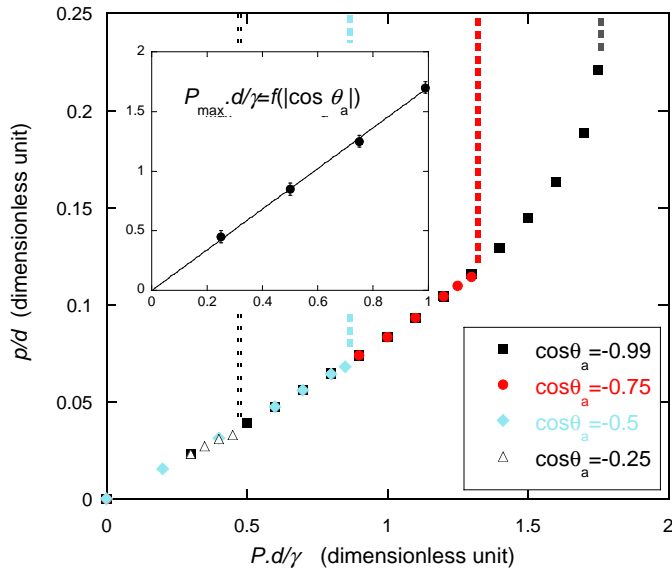


**Fig. 9.** Calculated penetration *versus* Laplace pressure on a perfect array for four contact angles. For all the numerical results, the lengths and the pressures are normalized by  $d$  and  $\gamma/d$ , respectively. The dashed lines represent the value at which the calculation diverges for the different surfaces. For all surfaces,  $r = 0.2d$ , only the value of  $\theta_a$  is changed. Inset: maximal pressure as a function of  $|\cos\theta_a|$ . The full line corresponds to equation (3) which correctly predicts the dependence of  $P_{\text{sliding}}$  on  $\cos\theta_a$ .

with a contact line detached from the pillars edge. This defines the sliding pressure  $P_{\text{sliding}}$ .

In the low-pressure regime (regime I), the penetration curve inferred from the exact resolution of the Laplace equation is in rather good agreement with our experimental findings on perfect pillars arrays, see Figure 7. In addition,  $P_{\text{sliding}}$  yields a quantitative estimate of the pressure above which the pillars start impaling the liquid. However, this simple picture cannot account for several important features of the penetration scenarios observed in the experiments: the partly impaled states (regime II) cannot be described since it predicts that the penetration undergoes a discontinuous divergence as  $P_L$  exceeds  $P_{\text{sliding}}$ . Furthermore, this scaling model does not explain the high-pressure regime (III) in which the slope of the penetration curve decreases as the pressure increases, Figure 7B.

### 3.1 Effect of localized defects: partial impalement

The RICM pictures have shown that the partial impalement systematically nucleates on an isolated defect. In order to assess the influence of these defects on the penetration curve we have solved the Laplace equation on a  $4 \times 3$  lattice including one “defective pillar” with periodic boundary conditions. More precisely, we have considered two types of defects: i) missing pillars (geometrical defect) and ii) pillars with lower advancing contact angle (chemical defect). Again, the maximum penetration is extracted from the shape of the interface. Figure 10 gathers

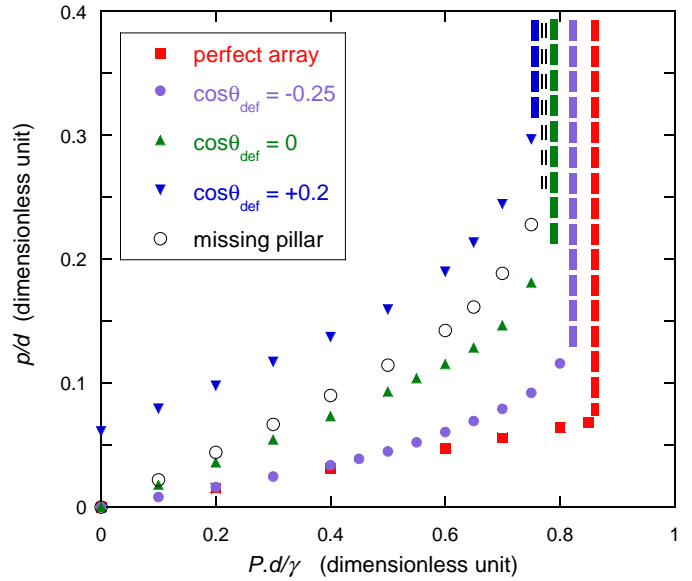


**Fig. 10.** Calculated penetration *versus* Laplace pressure for surfaces with different types of defect. The dashed lines represent the calculated sliding pressure.  $r = 0.2d$  and  $\theta_a = 120^\circ$  for the regular pillars.

the penetration curves for different kind of defects and reveals important differences with the previous homogeneous (mean field) case. Firstly, if the advancing contact angle on the defect is less than  $90^\circ$ , the penetration is non-zero at zero pressure. This suggests that a single wetting pillar can strongly destabilized fakir drops for small  $h$ . Secondly, for non-wetting pillars, the penetration curve is unaffected by the defect in the low-pressure limit. At low pressure, the contact angle on the less hydrophobic pillar has not reached its advancing value, the contact line remains pinned on the upper edge of the pillar. In turn, the shape of the interface and the penetration depth do not differ from the ones on a perfect array. When the Laplace pressure cannot be countered by the elementary force  $f$  on the defect (this is always the case for missing pillars), the local contact angle takes its advancing value and the contact line slides along this less hydrophobic pillar whereas the interface remains pinned on the top edge of the regular ones. The liquid is only partly impaled. Increasing the pressure we observe the growth of the partly impaled region, Figure 11, until it covers the twelve pillars. The sliding of the interface along all the pillars then leads to the Wenzel transition. A direct consequence of the partial impalement is the sharp increase of the slope of the penetration curve prior to the full penetration. This behavior correctly reproduces what is experimentally observed in the intermediate pressure regime (II) see Figure 7A.

We also stress on the weak dependence of the critical sliding pressure on the presence of defects in the limit of low defects density, Figure 10. Eventually, we mention that the range of pressure over which partial impalement is numerically observed increases with the box size. The calculation of the interface profile for a large number of pillars goes beyond the scope of this paper.

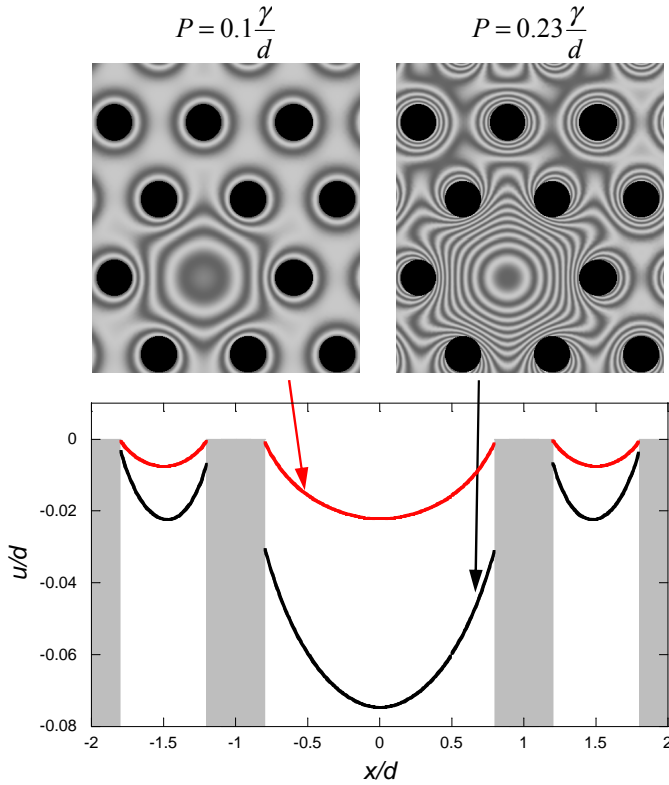


**Fig. 11.** Computed profiles and RICM patterns for a surface with one missing pillar. At  $P = 0.1\gamma/d$  the drop is in the fakir state: the surface is attached to edges of the pillars and adopts a tent fabric shape. At  $P = 0.23\gamma/d$ : the drop is partially impaled, the pillars close to the defect have penetrated the liquid. The partially impaled region covers almost the entire numerical box. The sliding transition occurs at  $P = 0.231\gamma/d$ . Here  $r = 0.2d$  and  $\theta_a = 98^\circ$ .

We have demonstrated that the partial impalement of the liquid interface can be correctly described within our simple framework by including geometrical or chemical heterogeneities of the patterned solid substrate. This allows for a description of the two first step of the impalement scenario identified on the experimental penetration curves and on the interface profiles (regime I and II). However, some ingredient seems to be still missing in our theoretical description to account for the last regime observed with the most robust superhydrophobic surface, namely the high-pressure regime where the slope of the penetration curve strongly decreases as the drop curvature increases.

### 3.2 Edge effects can save fakir droplets from impalement

The drop-substrate interface is connected to the macroscopic liquid-gas interface (the apparent part of the drop). At a macroscopic level, the two interfaces connect at the triple line where  $u = 0$ . The RICM observations show that the drop always contacts the top of the pillars located along the contact line, see Figure 4. Moreover, the

profiles plotted on Figure 6 clearly show that the macroscopic contact line pulls the interface upward and thus locally impedes drop impalement.

So far, restricting our model to periodic interfaces, we have implicitly ignored any potential edge (finite size) effect on the drop shape. Obviously, a complete description of the wetting behaviour of a drop would require the full knowledge of the interface's shape at all scales [22]. Instead, we now propose a minimal model to rationalize the stabilization of the fakir state due to the finite size of the “liquid-substrate” contact surface. We adopt a simplified continuous description of the partly impaled liquid interface. However, one have to keep in mind that, in our experiments, only few tens of pillars support the fakir drop in the late stage of the partial impalement (regime III). Balancing all the forces acting on the free surface, the drop Laplace pressure, the surface tension and the coarse-grained capillary force applied by all the partly wetted pillars, we infer the equilibrium condition for the coarse-grained penetration field  $\langle u \rangle$  in the small deformations limit:

$$(1 - \phi)P - \gamma \Delta \langle u \rangle - \left\langle f \sum_n \delta(\mathbf{r} - \mathbf{r}_n) \right\rangle = 0, \quad (4)$$

with  $P$  is the pressure in the drop and where the partly wetted pillars are modeled by pointwise vertical forces of magnitude  $f = (2\pi r)\gamma \cos \theta_a$  located at the vertices  $\mathbf{r}_n$  of the lattice (the brackets stand for spacial averaging). In what follows we focus on the late stage of the impalement transition. All the pillars below the drop are supposed to have penetrated the liquid except at the macroscopic contact line. Consequently, the force applied by the wetted pillars does not depend on local shape of the interface and is equal to  $f\phi/(\pi r^2)$ . Therefore, the equilibrium condition for the averaged penetration field is

$$\gamma \Delta \langle u \rangle = (1 - \phi)(P - P_{\text{sliding}}), \quad (5)$$

where the sliding pressure has been defined in equation (3). This equation is solved with the boundary conditions  $\langle u \rangle = 0$  at the macroscopic contact line, *i.e.* at a distance  $R = R_d \sin \theta_{\text{fakir}}$  from the center of the circular liquid-solid interface. Using  $P = 2\gamma/R_d$ , it is then straightforward to compute the maximal penetration of the resulting parabolic profile:

$$p = \gamma(1 - \phi) \left( \frac{P - P_{\text{sliding}}}{P^2} \right) \sin^2 \theta_{\text{fakir}}. \quad (6)$$

Note that our experiments confirm that the interface profile is very well approximated by a paraboloid shape at large scale, Figure 6. The above theoretical penetration is plotted and compared to our experimental data in Figure 12. Clearly this model qualitatively captures the main feature of the third penetration regime for which the slope of the penetration curve decreases for  $P > P_{\text{sliding}}$ . Since at the onset of the Wenzel transition the drop is only supported by  $\sim 30$  pillars, we cannot expect more than a qualitative agreement with the experiments. The three

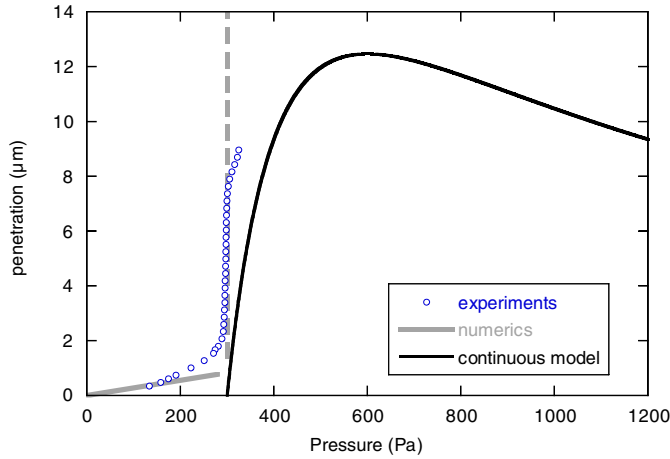


**Fig. 12.** Penetration *versus* pressure for a drop on a perfect array. The experimental data are compared to our theoretical predictions. Gray lines correspond to the mean-field model solved numerically. The equation of the black curve is given by equation (6) with  $\theta_{\text{fakir}} = 150^\circ$  and  $P_{\text{sliding}} = 293$  Pa. This last value is consistent with a sliding pressure calculated for an advancing contact angle  $\theta_a = 98^\circ$  (dashed gray line). According to this simplified model, pillars longer than  $14 \mu\text{m}$  should prevent the impalement of arbitrarily small droplets.

penetration regimes are now correctly described, taking into account both spatial heterogeneities on the surface and the finite size of the droplet.

We now highlight a more surprising effect, that should be observed on very slender pillars. Indeed, the model presented above actually predicts another unexpected penetration regime. Equation (6) tells us that the penetration could in principle reach a maximal value at  $P = 2P_{\text{sliding}}$ :

$$p_{\text{max}} = (1 - \phi) \frac{\gamma \sin^2 \theta_{\text{fakir}}}{4P_{\text{sliding}}}. \quad (7)$$

Above  $2P_{\text{sliding}}$ ,  $p$  decreases asymptotically to zero. Consequently, if the pillars height  $h$  exceeds  $p_{\text{max}}$ , the drop would never reach the Wenzel state and remain in the fakir state even for arbitrarily small radius! This surprising result can be understood by keeping in mind that the smaller the drop the more  $P_L$  pushes the interface downwards, but also that, the smaller the drop, the more volume conservation hinders the drop penetration. We note that at  $P = 2P_{\text{sliding}}$  the drop radius is equal to  $4p_{\text{max}}(1 - \phi)/\sin^2 \theta_{\text{fakir}}$  and can thus be much larger than  $p_{\text{max}}$  since fakir drops are associated with very high contact angles. Unfortunately, we did not manage to construct PDMS pillars of sufficiently high aspect ratio to observe the “immortal” fakir droplets. Nevertheless, this prediction is consistent with experiments done on carbon nanotube forests on which micron size droplets remains in the fakir state [23]. We also mention that recent experiments performed on ultra thin and ultra high microfabricated silicon pillars have confirmed this counterintuitive theoretical prediction [24].

In summary, we have combined a local and a coarse-grained description of the wetting states observed exper-

imentally on superhydrophobic surfaces. Thanks to the simple local model solved numerically, we have identified the physical mechanisms that dictate the pressure-induced transitions between these wetting states. We have demonstrated that localized defects (chemical or geometrical heterogeneities) play an important role in the nucleation and growth scenario that leads to the transition between the fakir and the partly impaled state. We emphasize that this model is appropriate whatever the mechanisms responsible for the pressure increase (gravity, drop squeezing, electrostatic pressure, ...). We have also revealed the importance of the finite size of the interface at high pressure. We have especially shown that surfaces patterned with very slender pillars can support arbitrarily small droplets, *i.e.* droplets with arbitrarily high Laplace pressure. Eventually, we precise that the simple picture proposed in this section is appropriate to describe the robustness of both stable or metastable fakir states since in our analysis we did not assume that fakir drops minimizes their surface energy.

## 4 Conclusion: design strategies for robust non-wetting surfaces

We close this paper proposing some guidelines for the design of robust superhydrophobic surfaces. The main motivation concerns the construction of lab-on-a-chip devices capable of: i) avoiding Taylor dispersion effects when transporting multiple fluids [25]. This goal could be reached if liquids could flow in the channels with a flat velocity profile. Large slip length and thus flattened velocity profiles can be achieved in superhydrophobic microchannels [26]. ii) Transporting highly curved liquid droplets in microchannel or on open assays [27]. To avoid fouling and material loss the microfluidic droplets must not wet the channels’ walls. Superhydrophobic patterning could be used to achieve a geometric control of the wetting properties of the device without adding surfactant molecules [28]. For these two applications the ideal superhydrophobic device must be able to resist against impalement under the application of high pressures and exhibit an ultra low contact angle hysteresis for drop transport. The second requirement can be fulfilled reducing the pattern solid fraction (note that this would also increase the apparent slip length). Concerning the resistance against impalement that would irreversibly stick the drops on the surface or reduce the slip length to zero, we have learned from the penetration curves that the working pressure should be much lower than  $P_{\text{sliding}}$ . As a matter of fact, close to this critical value a small fluctuation of the pressure would lead to a sudden and large increase of the liquid penetration. To widen the range of working Laplace or hydrodynamic pressure  $P_{\text{sliding}}$  has to be as large as possible. Hence, for a given liquid fraction  $\phi$ , the size of the elementary pattern has to be as small as possible. It is worth mentioning that the slenderness of the pattern does not influence the value of  $P_{\text{sliding}}$ . For continuous phase flows, it is thus ineffectual to increase the height of the patterns above

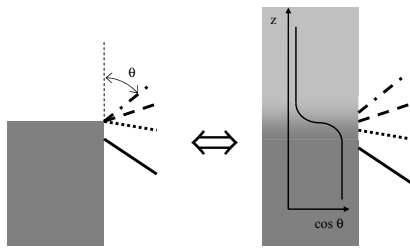


**Fig. 13.** Left: wetting behaviour on the edge of a pillar. The lines represent the interfaces for different contact angles. The interface connect the pillar at its corner for all angles smaller than  $\theta_a$ , when  $\theta = \theta_a$  (solid line), the interface can join the pillar side. Right: the simulated behaviour used in our calculation. The pillar is considered as an infinite cylinder along which the contact angle varies with  $z$ . The sharp variation of  $\cos \theta$  around  $z = 0$  mimics the effect of the pillar edge.

$h = p(P_{\text{sliding}})$ . But, we have shown that when the pillars aspect ratio exceeds  $(1 - \phi)/(8\phi \cos \theta_a \sin^2 \theta_{\text{fakir}})$  (see Eqs. (3) and (7)) droplets cannot fully wet and stick on the patterned substrate. Consequently, this high robustness against impalement could be put at work to design microfluidic devices able to transport and store ultra small surfactant free droplets.

We thank Soline Ngan, Abdou-Rachid Thiam and Alexis Prevost for help with the experiments. Mathilde Reyssat and David Quéré are acknowledged for the communication of experimental results prior to publication.

## Appendix A. Numerical resolution of the Laplace equation

We have used the open-source software Surface Evolver (SE) to solve the Laplace equation for the liquid interface in contact with the pillars array [29]. The surface is discretized in a mesh of triangular facets. A steepest descent procedure is then applied to find the lowest-energy conformation. In addition to the geometric boundary conditions, several constraints such as pressure, wetting properties, gravity can be imposed.

The numerical results presented in this paper obey to the following specifications:

- Computation box: the calculation in a mean-field approach is only calculated inside one lattice’s elementary cell of the periodic surface. This cell has been chosen to be parallelepipedic with periodic conditions along the  $x$  and  $y$  directions. Calculations for perfect arrays have been performed on elementary cells of lateral sizes  $d \times \sqrt{3}d$  containing 2 pillars. The role of defect has been investigated on  $3d \times 2\sqrt{3}d$  cells with 12 pillars including a single defect.
- Capillary pressure: the pressure  $P$  in the liquid is related to the curvature  $\mathcal{C}$  of the liquid-gas interface:  $P = \gamma\mathcal{C}$ . The effect of pressure is taken into account by imposing the value of the constant curvature of the surface.

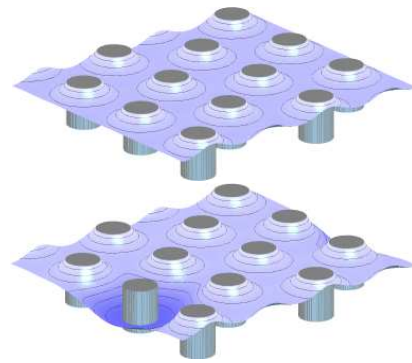


**Fig. 14.** Examples of a surface calculated for a perfect array (top) and for a cell with defective pillar on which the advancing contact angle is  $\theta_a = 90^\circ$  (bottom).

- Wetting properties: the calculations have to take into account two possible situations for the contact line around a pillar: i) The contact line is pinned on the top edge of the pillar, and the local contact angle can take any value smaller than  $\theta_a$  (see Fig. 13, left). ii) As  $\theta_a$  is reached, the contact line can take any position along the pillars. To bypass the difficulty of computing a sharp edge, we have modeled the pillars by a set of infinite cylinders along which the contact angle can undergo abrupt but continuous variations. The wetting properties vary with the height  $z$  like  $\cos \theta = \cos \theta_a \tanh(z/s)$  (see Fig. 13, right) where  $s$  is a typical size for the curvature of the pillars’ edge. In this model, a contact line at  $|z| < s$  is pinned on the edge of the pillar, while  $|z| \gg s$  means that the pillar penetrates inside the liquid (we have taken  $s = d/1000$ ). To model chemical heterogeneities, it is possible to assign a different value to  $\theta_a$  for each pillar, an example of localized chemical heterogeneity is shown in Figure 14.

## References

1. C. Neinhuis, W. Barthlott, *Ann. Bot.* **79**, 668 (1997).
2. X. Gao, L. Jiang, *Nature* **26**, 432 (2004).
3. W. Lee, M.K. Jin, W.C. Yoo, J.K. Lee, *Langmuir* **20**, 7665 (2004).
4. R. Blossey, *Nat. Mater.* **2**, 301 (2003).
5. X.M. Li, D. Reinhoudt, M. Crego-Calama, *Chem. Soc. Rev.* **36**, 1350 (2007).
6. X. Feng, L. Jiang, *Adv. Mater.* **18**, 3063 (2006).
7. M. Cailles, D. Quere, *Soft Matter* **1**, 55 (2005).
8. B. He, N.A. Patankar, J. Lee, *Langmuir* **19**, 4999 (2003).
9. A. Iafuma, D. Quere, *Nat. Mater.* **2**, 457 (2003).
10. U.T. Cheng, D.E. Rodak, *Appl. Phys. Lett.* **86**, 144101 (2004).
11. M. Reyssat, A. Pepin, F. Marty, Y. Chen, D. Quere, *Europhys. Lett.* **74**, 306 (2006).
12. D. Bartolo, F. Bouamrine, E. Verneuil, A. Buguin, P. Silberzan, S. Moulinet, *Europhys. Lett.* **74**, 299 (2006).
13. G. McHale, S. Aqil, N.J. Shirtcliffe, M.I. Newton, H.Y. Erbil, *Langmuir* **21**, 11053 (2005).
14. G. Carbone, L. Mangialardi, *Eur. Phys. J. E* **16**, 67 (2005).

15. C. Cottin-Bizone, C. Barentin, E. Charlaix, L. Bocquet, J.-L. Barrat, *Eur. Phys. J. E* **15**, 438 (2004).
16. C. Ishino, K. Okumura, D. Quere, *Europhys. Lett.* **68**, 419 (2004).
17. C. Ishino, K. Okumura, *Europhys. Lett.* **76**, 464 (2006).
18. N.A. Patankar, *Langmuir* **19**, 1249 (2004).
19. Y. Xia, G.M. Whitesides, *Angew. Chem. Int. Ed.* **37**, 550 (1998).
20. I. Langmuir, *Phys. Rev.* **12**, 368 (1918).
21. D. Quere, J.-M. di Meglio, F. Brochard-Wyart, *Rev. Phys. Appl.* **23**, 1023 (1988).
22. A. Dupuis, J.-M. Yeomans, *Langmuir* **21**, 2624 (2005).
23. K.K.S. Lau *et al.*, *Nano Lett.* **3**, 1701 (2003).
24. M. Reyssat, J.M. Yeomans, D. Quéré, to be published in *Europhys. Lett.* (2008).
25. H.A. Stone, A.D. Stroock, A. Ajdari, *Annu. Rev. Fluid. Mech.* **36**, 381 (2004) and references therein.
26. P. Joseph, C. Cottin-Bizonne, J.-M. Benoît, C. Ybert, C. Journet, P. Tabeling, L. Bocquet, *Phys. Rev. Lett.* **97**, 156104 (2006).
27. T.M. Squires, S.R. Quake, *Rev. Mod. Phys.* **77**, 977 (2005) and references therein.
28. A. Ajdari, M. Joannicot, *Science* **309**, 887 (2005).
29. <http://www.susqu.edu/facstaff/b/brakke/evolver/>.